



Precise control of the ionization channel in strong-field ionization by a few-cycle chirped laser pulseYue Sun , Zhuo Wang, Cheng-Wu Li, and Xue-Shen Liu**Institute of Atomic and Molecular physics, Jilin University, Changchun 130012, P. R. China* (Received 6 June 2022; revised 8 September 2022; accepted 9 September 2022; published 23 September 2022)

We investigate theoretically the photoelectron holography in strong-field ionization by a few-cycle chirped laser pulse. It is shown that the numerical results by solving the two-dimensional (2D) time-dependent Schrödinger equation (TDSE) are in agreement with that by using the semiclassical two-step (SCTS) model. The opening and the closing of the ionization channel can be controlled precisely by a few-cycle chirped laser pulse and the holographic interference structure can be isolated by adjusting the chirp parameters. This holographic interference structure is related to the rescattered electron wave packet (EWP) which released within an attosecond timescale. We demonstrate that the chirped laser pulse can be used to coherently control the recollision process. By analyzing the rescattered trajectory, we illustrate that the travel time of the rescattered electron is increased and the rescattered electron can obtain high return energy in a negatively chirped laser pulse. In addition, we also illustrate that the photoelectron momentum distributions (PMDs) are very sensitive to the carrier-envelope phase.

DOI: [10.1103/PhysRevA.106.033116](https://doi.org/10.1103/PhysRevA.106.033116)**I. INTRODUCTION**

Above-threshold ionization (ATI) [1–3], high-order harmonic generation (HHG) [4–6], and nonsequential double-ionization (NSDI) [7–9] are interesting nonlinear phenomena in strong-field ionization. These phenomena can be described by a three-step model [10]. In this model, the ionized electron wave packet (EWP) undergoes three processes, i.e., ionization, acceleration in the strong laser field, and return to the parent ion. The ionized EWP can directly reach the detector (known as direct trajectory) or return to the parent ion for rescattering (known as rescattered trajectory) [11]. The ionized EWPs emitted from different ionization time with the same final momentum will interfere with each other and then show the rich interference structures in the photoelectron momentum distributions (PMDs) [12–14].

In recent decades, the interference structures in the PMDs have become a very important topic in atomic or molecular physics. There are several common interference structures in the PMDs, for example, the ATI rings [15], the temporal double-slit interference structure [16] and the photoelectron holography [17]. The spider-like holographic interference structure was first observed in experiments [17]. The holographic interference structure stem from the interference between rescattered EWP and the direct EWP from the same quarter cycle of the laser field. Because the rescattered electron can record the time-resolved information about the parent ion, the photoelectron holography is considered as an ideal method to probe ultrafast atomic and molecular dynamics. Generally, the different kinds of interference structures will be superimposed in the PMDs [18]. Therefore, an isolated

holographic interference structure will be helpful to explore the dynamics of atoms and molecules [19–21].

The chirped laser pulse is an important tool to probe and control the ultrafast dynamics and has been widely used to investigate the nonlinear phenomena of strong-field ionization experimentally and theoretically [22,23]. In a chirped laser pulse, excited bound states [24] and the carrier-envelope phase (CEP) [25] all play crucial roles in the effect of the chirp on the ATI spectra. Nakajima [24] investigated theoretically that the origin of the chirp dependence in above-threshold ionization is the excited bound states, and they found that the excited bound states play a more important role than the ground state. Zille *et al.* [25] measured and demonstrated the CEP-dependent and chirp-dependent photoelectron spectra for few-cycle pulses. They found the stripe-like interference structures and illustrated the dependence of the stripe-like interference structures on the chirp of the laser pulse.

For ATI, the asymmetry of the electron yield in the momentum distributions is found to be very sensitive to a few-cycle chirped laser pulse for a fixed carrier-envelope phase. Peng *et al.* [26] investigated theoretically the PMDs of a H atom by chirped few-cycle attosecond pulses. They found the asymmetry of the electron yield in the momentum distributions is very sensitive to a few-cycle chirped laser pulse for a fixed carrier-envelope phase. Meanwhile, the asymmetry of the ionized electron in the momentum distributions is also sensitive to the carrier-envelope phase for a fixed chirp parameter. Xiang *et al.* [27] investigated theoretically the above-threshold ionization (ATI) of a hydrogen atom by solving one-dimensional time-dependent Schrödinger equation (TDSE). They found that the cutoffs of the first and second plateaus of the ATI spectra extend significantly with the different chirp parameters.

For HHG, a large number of studies show that the harmonic cutoff can be extended [28] and the ultrashort isolated attosecond pulse can be generated [29,30] in a chirped laser pulse.

*liuxs@jlu.edu.cn

The influence of the positively chirped laser pulse and the negatively chirped laser pulse on electron motion is different [31]. A positively chirped laser pulse is more efficient for population inversion than a negatively chirped laser pulse is for the photodissociation of H_2^+ [32]. For the few-cycle chirped laser pulse with CEP-stabilized and nonstabilized CEP, the negatively chirped laser pulse has a different modulation than the harmonic spectra [33].

In this paper, we investigate theoretically the photoelectron holography of a hydrogen atom in strong-field ionization by a few-cycle chirped laser pulse. We demonstrate that the PMDs in a negatively chirped laser pulse are more sensitive to the chirp parameters than those in a positively chirped laser pulse. In a negatively chirped laser pulse, the holographic interference structure on the attosecond timescale can be isolated by adjusting appropriate negative chirp parameter ($\beta = -2$). In addition, we also demonstrate that the chirped laser pulse not only can control precisely the opening or the closing of the ionization channel but also can be used to coherently control the recollision process. By analyzing the rescattered trajectory, we illustrate that the travel time of the rescattered electron is increased and the rescattered electron can obtain high return energy in a negatively chirped laser pulse. In addition, we also illustrate that the PMDs are very sensitive to the CEP. Our results may provide a reference for further research of the attosecond dynamics.

II. THEORETICAL MODEL AND COMPUTATIONAL METHODS

To better explain the dynamic process in strong field physics, many theoretical methods have been developed. For example, the simple-man model, time-dependent Schrödinger equation method and semiclassical model, etc. Although the simple-man model can explain many physical phenomena qualitatively, there are still some differences between the simple-man model and other theoretical methods including Coulomb potential. In this paper, we mainly illustrate the precise control of the ionization channel by adjusting the chirped laser pulses, and then isolate the spider-like holographic interference structure. In this section, we briefly introduce the two-dimensional (2D) TDSE method and the two-dimensional semiclassical two-step (SCTS) model [34]. We use atomic units throughout this paper.

A. Time-dependent Schrödinger equation method

The two-dimensional time-dependent Schrödinger equation (TDSE) in the length gauge is given by

$$i \frac{\partial \psi(\vec{r}, t)}{\partial t} = H(\vec{r}, t) \psi(\vec{r}, t), \quad (1)$$

where $r = (x^2 + y^2)^{1/2}$ is the distance between the ionized electron and the nucleus and $H(\vec{r}, t)$ is the Hamiltonian of an atomic system interacting with a laser pulse in the limit of the dipole approximation and single-active-electron approximation. It can be written as

$$H(\vec{r}, t) = \frac{\vec{p}^2}{2} + V(\vec{r}) + \vec{r} \cdot \vec{E}(t), \quad (2)$$

where \vec{p} is the electronic momentum. $V(\vec{r}) = -1/(x^2 + y^2 + a)^{1/2}$ is the effective soft-core potential. The soft-core parameter $a = 0.65$ is used to eliminate the singularity of the potential function at the origin. The ionization potentials of the ground state evolved by the imaginary-time evolution method are $I_p = 0.5$ a.u., which corresponds to the energy of the ground state of the H atom. $\vec{E}(t)$ is the electric field of the laser pulse and $\vec{r} \cdot \vec{E}(t)$ is the laser-atom interaction.

The two-dimensional TDSE has been solved by fast Fourier transform technique combined with split-operator method [35]. We use the imaginary-time evolution method to obtain the initial wave function and the grid size is 1200 a.u., the time step of propagation is $\Delta t = 0.05$ a.u. The final momentum distribution can be obtained by projecting the final wave function into momentum space [36].

The form of the laser field is

$$E(t) = E_0 \cos[\omega t + \phi(t) + \varphi] f(t) \hat{x}, \quad (3)$$

where $E_0 = 0.0533$ a.u. is the field amplitude, $\phi(t) = \beta[(t - t_0)/\tau_0]^2$ is the phase of the chirped laser pulse, β is the chirp parameter of the pulse, $t_0 = 198$ a.u. is used to adjust the sweep range of the electric field, and $\tau_0 = 210$ a.u. is the parameter of controlling the steepness of the chirped function [30]. φ is the carrier-envelope phase, $f(t) = \sin^2(\frac{\pi t}{nT})$ is the envelope pulse with the parameter $n = 4$, $T = \frac{2\pi}{\omega}$ is the optical period, $\omega \approx 0.046$ a.u. is the laser frequency, and \hat{x} is the laser polarization direction.

B. Semiclassical two-step model

We also apply the two-dimensional semiclassical two-step (SCTS) model to investigate the photoelectron momentum distribution. Before introducing the SCTS model, we briefly introduce the two-dimensional quantum trajectory Monte Carlo (QTMC) method [37]. The advantage of the QTMC model is that the Coulomb effect on electron trajectories and interference patterns are fully considered based on the Feynman's path-integral approach. The phase information of each electron is given. It can well reconstruct the photoelectron momentum distribution and photoelectron angular distributions measured experimentally for above-threshold ionization. For the SCTS model, the phase information of the electron trajectory is modified based on the QTMC model. The two key ingredients of the SCTS model are the choice of an initial momentum distribution in the first tunneling step and a proper semiclassical description for the second step. Shvetsov-Shilovski *et al.* [34] use the expression of transition matrix element of the semiclassical propagator to describe the second step. The advantage of the SCTS model is that the low-energy angular structure of the photoelectron momentum distribution can be well reconstructed after the phase correction [34].

The electron first tunnels out of an atom and then the electron motion in the Coulomb and laser fields is described by the Newton equations

$$\ddot{\vec{r}}(t) = \frac{-\vec{r}(t)}{r^3(t)} - \vec{E}(t), \quad (4)$$

where $\vec{E}(t)$ is introduced in Eq. (3). For the two-dimensional semiclassical model, we use the real Coulomb potential due to the single ionization. In a two-dimensional $P_x \times P_y$ plane, the probability of a given final momentum is determined by adding coherently the trajectories in that bin

$$|A|_{\text{bin}}^2 = \left| \sum_j \sqrt{W(t_0, v_{0,\perp})} \exp(-i\Phi) \right|^2, \quad (5)$$

where j denotes the j th ionized electron trajectory, $W(t_0, v_{0,\perp})$ denotes the Ammosov-Delone-Krainov (ADK) rate [38,39]

$$W(t_0, v_{0,\perp}) \sim \exp\left[-\frac{2k^3}{3E(t_0)}\right] \exp\left[-\frac{kv_{0,\perp}^2}{E(t_0)}\right], \quad (6)$$

where $k = \sqrt{2I_p}$.

In the QTMC model, the trajectory phase for each electron is

$$\Phi = I_p t_0 - \int_{t_0}^{\infty} \left[\frac{v(t)^2}{2} - \frac{Z}{r(t)} \right] dt, \quad (7)$$

where $v(t)$ is the ionized electron velocity, I_p is the ionization potential and Z is the ion charge.

For the trajectory phase of each electron, Shvetsov-Shilovski *et al.* came up with a SCTS model. We can find the specific description of the SCTS model in Ref. [34], the phase can be modified as

$$\Phi = -v_0 r_0(t_0) + I_p t_0 - \int_{t_0}^{\infty} \left[\frac{v(t)^2}{2} - \frac{2Z}{r(t)} \right] dt, \quad (8)$$

where v_0 denotes the initial velocity, t_0 denotes the ionization time. We use the phase of Eq. (8) to investigate the ionization process in a chirped laser pulse.

III. RESULTS AND DISCUSSIONS

Figures 1(a)–1(c) show the electric field (blue dashed line) and the ionization rate (red solid line) of a H atom for a negatively chirped laser pulse ($\beta = -2$), a chirp-free laser pulse ($\beta = 0$), and a positively chirped laser pulse ($\beta = 2$), respectively, where the carrier-envelope phase is set as $\varphi = 0$. For a chirp-free laser pulse, the frequency of the laser pulse is uniform, as shown in Fig. 1(b). For a negatively chirped laser pulse, the frequency of the laser pulse changes from high frequency to low frequency, as shown in Fig. 1(a). On the contrary, for a positively chirped laser pulse, the frequency of the laser pulse changes from low frequency to high frequency, as shown in Fig. 1(c).

The ionization rate shown in Figs. 1(a)–1(c) is calculated by the ADK theory [38,39]. Because the dependence between the ionization rate and the field amplitude is exponential, as indicated in Eq. (6), the ionization rate will significantly change with a small change of the amplitude of the laser field. When a H atom is exposed to a chirp-free laser pulse ($\beta = 0$), the electronic wave packet (EWP) is dominantly generated at the times t_1 , t_2 , and t_3 , as shown in Fig. 1(b). They are three different ionization channels. By adjusting the chirp parameter to $\beta = -2$, the pulse is negatively chirped as shown in Fig. 1(a). From Fig. 1(a), we can see that the ionization channels t_1 and t_2 are opened and the ionization

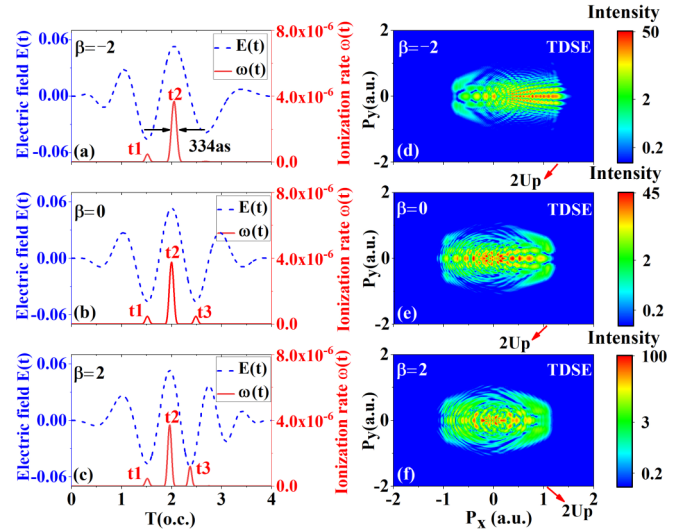


FIG. 1. (a)–(c) Electric field of the few-cycle laser pulse (blue dashed line) and ionization rate (red solid line) of a H atom for different chirp parameters. (d)–(f) The corresponding PMDs in the (p_x, p_y) plane in logarithmic scale by solving the TDSE. The laser pulse has a central carrier frequency $\omega \approx 0.046$ a.u., the laser field amplitude is $E_0 = 0.0533$ a.u., the carrier-envelope phase is $\varphi = 0$, the duration of the laser field is $n = 4$ and $t_0 = 198$ a.u., $\tau_0 = 210$ a.u.

channel t_3 is closed, which is because that the pulse peak around the channel t_3 is weakened. However, for a positively chirped laser pulse ($\beta = 2$), Fig. 1(c) shows that the ionization channel t_3 is enhanced due to the enhanced pulse peak around the channel t_3 . Thus we can control precisely the opening or the closing of the ionization channel t_3 by adjusting different chirp parameters.

Figures 1(d)–1(f) show the corresponding PMDs of a H atom in the (p_x, p_y) plane by solving the TDSE based on the ground state for a negatively chirped laser pulse ($\beta = -2$), a chirp-free laser pulse ($\beta = 0$) and a positively chirped laser pulse ($\beta = 2$), respectively. Nakajima [24] indicated that for the multiphoton ionization, the excited bound state plays a more important role than the ground state, since the ionization takes place through near-resonant intermediate states. However, for the tunneling ionization and barrier suppression ionization, the ionization is mainly induced by the ground state. In this paper, we mainly investigate the PMDs in the tunneling ionization regime.

For a chirp-free laser pulse, Fig. 1(e) shows that the PMDs are distributed in the region of $p_x \in [-1.0$ a.u., 1.0 a.u.] and exhibit the rich interference structures, which are the temporal double-slit interference structure [16] and the spider-like holographic interference structure [17]. For a negatively chirped laser pulse, the PMDs have obvious changes, as shown in Fig. 1(d). The PMDs are mainly distributed in the region of $p_x \in [-0.5$ a.u., 1.5 a.u.]. The holographic interference structure can be isolated from various interference structures and extending to higher-energy region. From Fig. 1(d), we clearly observe that the PMDs can reach $p_x = 1.5$ a.u. Figure 1(d) also shows a number of spots in the holographic interference structure. The red arrows denote the location of the $2U_p$.

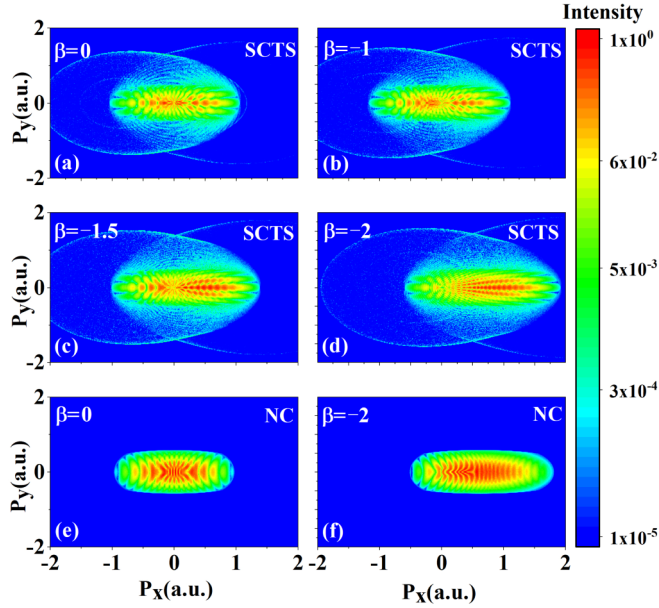


FIG. 2. PMDs in the (p_x, p_y) plane in a logarithmic scale for different negative chirp parameters by using the SCTS model. (a) $\beta = 0$, (b) $\beta = -1$, (c) $\beta = -1.5$, (d) $\beta = -2$. (e), (f) PMDs of H atom for (a) the chirp-free laser pulse ($\beta = 0$) and (d) the negatively chirped laser pulse ($\beta = -2$) by using the simple-man model (i.e., non-Coulomb potential, NC). The laser pulse has a central carrier frequency $\omega \approx 0.046$ a.u., the laser field amplitude is $E_0 = 0.0533$ a.u., the carrier-envelope phase is $\varphi = 0$, the duration of the laser field is $n = 4$, and $t_0 = 198$ a.u., $\tau_0 = 210$ a.u.

$U_p = \frac{E_0^2}{4\omega^2}$ is the ponderomotive potential, where E_0 denotes the field amplitude and ω denotes the laser frequency.

For a positively chirped laser pulse, Fig. 1(f) shows that the PMDs are still distributed in the region of $p_x \in [-1.0 \text{ a.u.}, 1.0 \text{ a.u.}]$ and the ring-like structure gradually appears, which is produced by the EWPs emitted exactly one or more laser cycles. The appearance of the ring-like structure is due to the enhancement of the channel t_3 , so that the ionized electrons from the channel t_1 and the channel t_3 can interfere with each other. The ring-like interference structure will interfere with spider-like holographic interference structure as shown in Fig. 1(f). For a negatively chirped laser pulse, ionization channel t_3 is closed as shown in Fig. 1(a), it is more conducive to isolate spider-like holographic interference structure as shown in Fig. 1(d). In this paper, we illustrate the PMDs in a negatively chirped laser pulse in detail.

In Fig. 2, we turn to SCTS model to understand the holographic interference structure appearing in the positive direction for the negatively chirped laser pulse. Figures 2(a) and 2(d) show the PMDs for the $\beta = 0$ and $\beta = -2$, respectively, which are in good agreement with the TDSE results as shown in Figs. 1(e) and 1(d). Figures 2(a)–2(d) show that the symmetry of the PMDs region is destroyed, the interference structure of the negative direction can be suppressed, the spider-like holographic interference structure of the positive direction gradually dominates and the region of the PMDs can be expanded with the increase of the negative chirp parameter. It indicates that the electrons can obtain high energy in the negatively chirped laser pulse. When the negative chirp

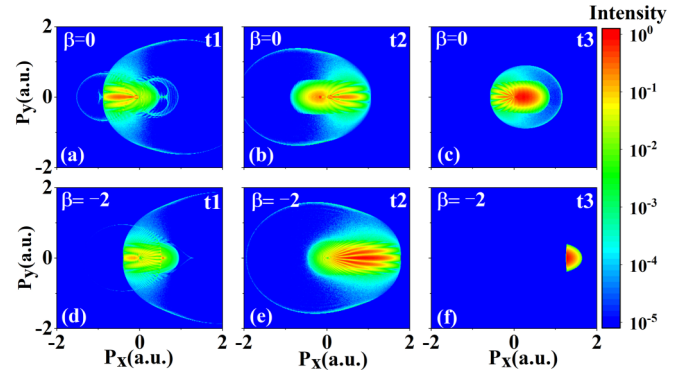


FIG. 3. PMDs of the EWPs which released from different ionization channels t_1 , t_2 , and t_3 for different chirp parameters. (a)–(c) The chirp-free laser pulse ($\beta = 0$). (d)–(f) The negatively chirped laser pulse ($\beta = -2$).

parameter $\beta = -2$, the holographic interference structure can be isolated in the positive direction, as shown in Fig. 2(d).

Figures 2(e) and 2(f) show the photoelectron momentum distributions by using the simple-man model (i.e., non-Coulomb potential, NC) for the chirp-free laser pulse ($\beta = 0$) and the negatively chirped laser pulse ($\beta = -2$), respectively. From Fig. 2(e), we find that the photoelectron momentum distributions are distributed in the region of $p_x \in [-1.0 \text{ a.u.}, 1.0 \text{ a.u.}]$, which agrees with the TDSE results [Fig. 1(e)] and SCTS model results [Fig. 2(a)]. However, many details are different for the different methods. For example, for Fig. 2(e), it only exhibits the temporal double-slit interference structure, which originates from the interference of the direct trajectory and the indirect trajectory. The spider-like holographic interference structure disappears. Similarly, Fig. 2(f) shows that the photoelectron momentum distributions are distributed in the region of $p_x \in [-0.5 \text{ a.u.}, 1.5 \text{ a.u.}]$. The region of the photoelectron momentum distributions corresponds well with the TDSE results [Fig. 1(d)] and SCTS model results [Fig. 2(d)]. But many details of the inner interference structures (for example, the spider-like holographic interference structure) are still invisible. Thus we mainly investigate the PMDs by using the SCTS model.

Due to the fact that the shape of the laser field and the ionization channel will be modulated precisely by adjusting the chirp parameters as shown in Figs. 1(a)–1(c). Figs. 3(a)–3(c) show the PMDs of the EWP which released from the ionization channels t_1 , t_2 , and t_3 for a chirp-free laser pulse ($\beta = 0$), respectively. From Figs. 1(a)–1(c), we can see that the EWP from the ionization channel t_1 is emitted within 1.3–1.6 T, the EWP from the ionization channel t_2 is emitted within 1.8–2.2 T and the EWP from the ionization channel t_3 is emitted within 2.3–2.6 T. From Figs. 3(a) (the ionization channel t_1) and 3(c) (the ionization channel t_3), we can clearly observe the spider-like holographic interference structures in the negative direction. The spider-like holographic interference structure in the positive direction originates from the EWP ionized from the ionization channel t_2 can be observed as shown in Fig. 3(b).

Figures 3(d)–3(f) show the PMDs of the EWP which released from three different ionization channels for a negatively

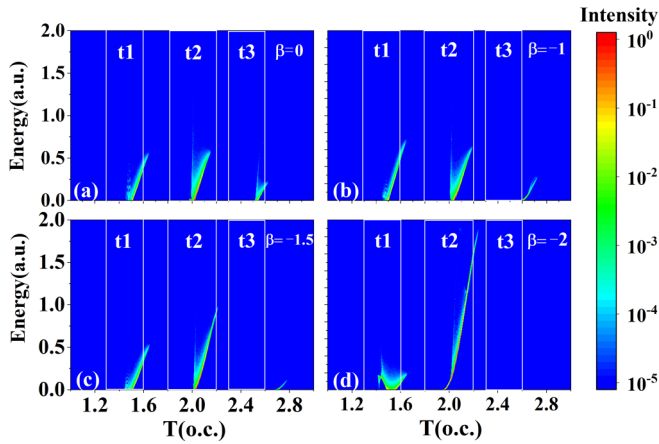


FIG. 4. Energy distribution of the rescattering electrons with respect to the ionization time for different negative chirp parameters. (a) $\beta = 0$, (b) $\beta = -1$, (c) $\beta = -1.5$, (d) $\beta = -2$. The white solid line frames denote the different ionization channels t_1 , t_2 , and t_3 , respectively.

chirped laser pulse ($\beta = -2$). From Fig. 1(a), we know that the ionization channels t_1 and t_2 are opened, and the ionization channel t_3 is closed for the chirp parameter $\beta = -2$. In Fig. 3(d) (the ionization channel t_1), it exhibits the inner spider interference structure in the low-energy region on the positive direction of the PMDs. The inner spider structure in the low-energy region comes from the interference of the direct trajectories and the multiple forward-scattering trajectories [40,41]. From Fig. 3(e) (the ionization channel t_2), we can find the isolated spider-like holographic interference structure with high energy in the positive direction.

Through the above analysis, it implies that the isolated spider-like holographic interference structure shown in Fig. 1(d) comes from the ionization channel t_2 for a negatively chirped laser pulse ($\beta = -2$). And the spots in the holographic interference structure shown in Fig. 1(d) originate from the interference between the electrons from the ionization channels t_1 and t_2 . From Fig. 1(a), we can see that the EWP from the ionization channel t_2 is emitted within an attosecond timescale around 334 as, which may be used to probe the attosecond ultrafast dynamics. However, Fig. 3(f) does not show any interference fringes. It indicates that the ionization channel t_3 has little contribution to the PMDs for the chirp parameter $\beta = -2$, which is in agreement with the closing of the ionization channel t_3 shown in Fig. 1(a).

We know that the final energy of the electrons is dependent on the initial ionization time [21,42], and the rescattering electrons play an important role in the holographic interference structure. To clarify the physical mechanism of the spider-like holographic interference structure as shown in Figs. 1(d) and 3(e), we demonstrate the energy distribution of the rescattering electrons with respect to the ionization time for different negative chirp parameters, as shown in Fig. 4. The white solid line frames denote the different ionization channels t_1 , t_2 , and t_3 , respectively.

The electron trajectories can be classified as the direct trajectory and the rescattered trajectory according to the effect of the Coulomb potential on them [21,43,44]. If $p_{\perp}v_{\perp 0} > 0$

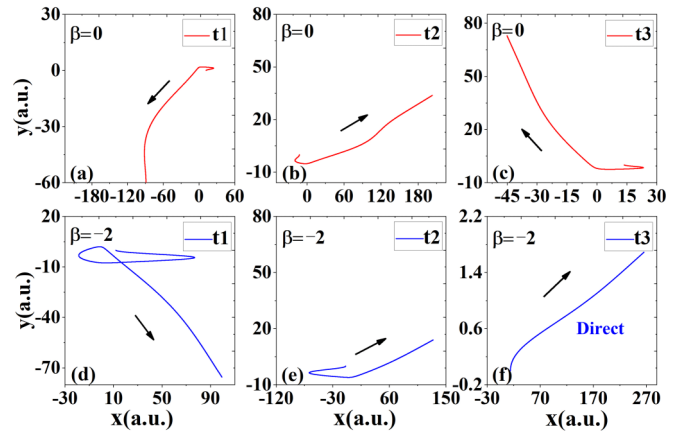


FIG. 5. Typical trajectories of the rescattered electrons ionized from different ionization channels and different chirp parameters. (a)–(c) $\beta = 0$ (red line). (d)–(f) $\beta = -2$ (blue line).

(where p_{\perp} is the final perpendicular momentum and $v_{\perp 0}$ is the initial velocity), the Coulomb potential is weak and not enough to change the perpendicular direction of the electron trajectory. This type of ionized trajectory is called the direct trajectory. Similarly, if $p_{\perp}v_{\perp 0} < 0$, the Coulomb potential is strong, and this type of ionized trajectory is called the rescattered trajectory.

As shown in Fig. 4, we can observe that there is a little change of the final energy of the rescattered electrons ionized in the ionization channel t_1 with the increase of the negative chirp parameter. For the ionization channel t_2 , the final energy of the rescattered electrons is much higher in the negatively chirped laser pulse ($\beta = -2$) shown in Fig. 4(d) than that in the chirp-free pulse ($\beta = 0$) shown in Fig. 4(a). It can be seen from Fig. 4(d) that the maximum energy can reach to energy ≈ 1.6 a.u. in the ionization channel t_2 . We know that the few-cycle laser pulse is restricted by the envelope pulse. As shown in Fig. 1(a), we can clearly observe that the field amplitude in the ionization channel t_2 is higher than the field amplitude in the ionization channel t_1 . Thus the ionized electrons can obtain higher energy in the ionization channel t_2 . It is proved once again that the ionized rescattered electrons can obtain higher energy in the negatively chirped laser pulse shown in Figs. 1(d) and 3(e). For the ionization channel t_3 , the rescattered electrons disappeared with the increase of the negative chirp parameter, as shown in Fig. 4.

To better illustrate that the rescattered electrons can obtain higher energy in the ionization channel t_2 for a negatively chirped laser pulse shown in Fig. 4(d), we trace the classical trajectories of the rescattered electrons for different ionization channels (i.e., t_1 , t_2 , t_3) and different chirp parameters $\beta = 0$ (red line) and $\beta = -2$ (blue line) as shown in Fig. 5. Figures 5(a) and 5(d) show the rescattered trajectories, which are released from the ionization channel t_1 . In Fig. 5(a) ($\beta = 0$), we can find the electron first move to the positive direction of the x axis and then return to the parent ion for a single forward rescattering. The interference of this rescattered trajectory and the direct trajectory can generate the spider-like holographic interference structure in the negative direction, which explains the phenomenon as shown in Fig. 3(a). When the chirp

parameter $\beta = -2$, as shown in Fig. 5(d), the electron is multiple forward scattering. It well proves the appearance of the inner spider holographic interference structure shown in Fig. 3(d).

Figures 5(b) and 5(e) show the rescattered trajectories, which are emitted from the same ionization channel t_2 but different chirp parameters. From Figs. 5(b) and 5(e), we find that the rescattered electrons all move to the negative direction of the x axis and then return to the parent ion for a single forward rescattering. The corresponding spider-like holographic interference structures will be generated in the positive direction, which explain the phenomena as shown in Figs. 3(b) and 3(e). It is worth noting that the region of holographic interference structure can be expanded as shown in Fig. 3(e), i.e., the electron can obtain the high energy in a negatively chirped laser pulse ($\beta = -2$), as shown in Fig. 4(d).

By comparing Fig. 5(b) with Fig. 5(e), we observe that the distance of the rescattered electron moving in the laser field (i.e., the travel time) is different. For the chirp-free laser pulse ($\beta = 0$), the rescattered electron ionized at the channel t_2 moves to $x \approx -25$ a.u. and then return to the parent ion as shown in Fig. 5(b). However, for the negatively chirped laser pulse ($\beta = -2$), Figure 5(e) shows that the rescattered electron ionized at the channel t_2 can moves to $x \approx -75$ a.u., i.e., the rescattered electron experiences a longer time acceleration when returning to the parent ion. The longer the travel time is, the higher kinetic energy the rescattered electron obtain from the driving laser field before the laser field reverses [30]. Therefore, the electron can obtain the high energy and the region of the holographic interference structure can be expanded as shown in Figs. 3(e) and 4(d).

Similarly, Fig. 5(c) shows that the rescattered electron ionized at the channel t_3 for the chirp-free laser pulse ($\beta = 0$). The interference of this rescattered trajectory and the direct trajectory can generate the spider-like holographic interference structure in the negative direction, which explains the phenomenon as shown in Fig. 3(c). From Figs. 3(f) and 4(d), we know that the ionization channel t_3 has little contribution to the PMDs and there is no rescattered trajectory at the ionization channel t_3 for the chirp parameter $\beta = -2$. Therefore, Fig. 5(f) shows a direct trajectory for the negatively chirped laser pulse ($\beta = -2$). Through statistical analysis, we also find that there are very few direct trajectories at the ionization channel t_3 for $\beta = -2$. This phenomenon proves once again that the channel t_3 is closed in the negatively chirped laser pulse ($\beta = -2$), which is in good agreement with that illustrated in Figs. 1(a), 3(f) and 4(d).

Through above analysis, we demonstrate that the chirped laser pulse not only can control precisely the opening or the closing of the ionization channel, but also can be used to coherently control the recollision process. To better understand the effect of the chirped laser pulse on the recollision process, the dependence of the return energy of the electron on the rescattering time are presented in Fig. 6 based on the three-step model [10]. Figures 6(a) and 6(b) show the return energy with respect to the rescattering time for the chirp-free laser pulse ($\beta = 0$) and the negatively chirped laser pulse ($\beta = -2$). The blue solid line frames denote different ionization channels t_1 , t_2 , and t_3 , respectively. By comparing Fig. 6(a) with Fig. 6(b), we can find that the return energy

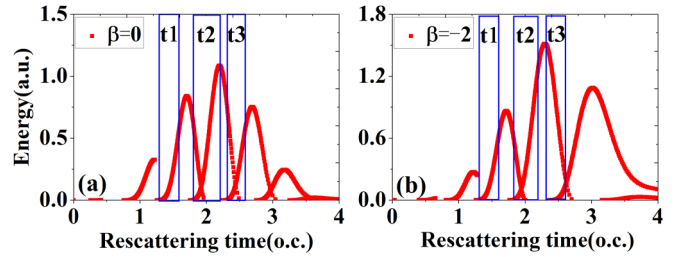


FIG. 6. Return energy of the electron as a function of the rescattering time for different chirp parameters (a) $\beta = 0$, (b) $\beta = -2$. The blue solid line frames denote different ionization channels t_1 , t_2 , and t_3 , respectively.

and the rescattering time of the ionized rescattered electron through the ionization channel t_1 have a slight change with the increase of the negative chirp parameter.

For the ionized rescattered electrons through the channel t_2 , the return energy with respect to the rescattering time dramatically changes with the increase of the negative chirp parameter. For the chirp-free pulse ($\beta = 0$), Fig. 6(a) shows that the return energy of the rescattered electron (energy ≈ 1 a.u.) for the channel t_2 . When the chirp parameter $\beta = -2$, Fig. 6(b) shows that the rescattered electron experiences a longer time acceleration when returning to the parent ion and can obtain high return energy (energy ≈ 1.5 a.u.). Xiang *et al.* [27] found that the cutoffs of the first and second plateaus of the ATI spectra extend significantly (i.e., energy enhancements) with the different chirp parameters. However, the rescattering electron may have little contribution to high-order ATI spectrum due to the weak field strength. For example, In Fig. 2(c) of Ref. [27], it is shown that the rescattering electrons with high energy have little contribution to high-order ATI spectrum due to the weak field strength. In our paper, we only investigate the motion of the rescattering electron and our parameters are different from those selected in Ref. [27]. It will cause differences in the laser pulse. From Fig. 1(a), we know that the field strength and the ionization rate in the ionization channel t_2 is higher than that in the ionization channel t_1 . Thus, the rescattering electrons with high energy in the ionization channel t_2 have great contribution to PMDs. The rescattered electron born at the channel t_3 never returns to its parent ion as shown in Fig. 6(b). It is proved once again that the travel time of the rescattered electron is increased and the rescattered electron can obtain high return energy in a negatively chirped laser pulse.

For a few-cycle chirp laser pulse, Peng *et al.* [26] and Zille *et al.* [25] investigate the influence of the chirp parameter and the CEP of the laser pulse. They found that the motions of the ionized electrons are very sensitive to the CEP. Therefore, we also investigate the PMDs of a H atom with different CEPs for a fixed chirp parameter $\beta = -2$, as shown in Fig. 7. Figures 7(a) and 7(b) show the electric field (blue dashed line) and the ionization rate (red solid line) for the CEP $\varphi = 0.25\pi$ and $\varphi = 0.5\pi$, respectively. From Figs. 7(a) and 7(b), we can find that the ionization time (i.e., ionization channels) of the electronic wave packet (EWP) also can be controlled precisely by adjusting different CEPs for a fixed chirp parameter. From Fig. 7(a), we can see that the ionization channels t_2 , and t_3 are

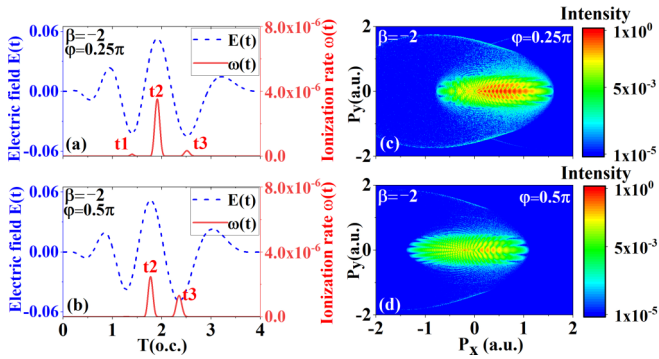


FIG. 7. Electric field of the few-cycle laser pulse (blue dashed line) and ionization rate (red solid line) of a H atom for a fixed chirp parameter $\beta = -2$ with different CEPs (a) $\varphi = 0.25\pi$, (b) $\varphi = 0.5\pi$. Panels (c) and (d) show the corresponding PMDs by using the SCTS model.

opened and the ionization channel t_1 is weak for $\varphi = 0.25\pi$. When the CEP is further increased to $\varphi = 0.5\pi$, as shown in Fig. 7(b), the ionization channel t_1 is closed and only the ionization channels t_2 and t_3 are opened. And the ionization rate of the ionization channel t_3 is also strong.

Figures 7(c) and 7(d) show the corresponding PMDs by using the SCTS model for the CEP $\varphi = 0.25\pi$ and $\varphi = 0.5\pi$, respectively. It can be seen that the PMDs are very sensitive to the CEP. Figure 7(c) shows that the PMDs are also mainly distributed in the region of $p_x \in [-0.5 \text{ a.u.}, 1.5 \text{ a.u.}]$ for $\varphi = 0.25\pi$. The holographic interference structure can also be isolated from various interference structures and extended to higher-energy region, which is similar to the results illustrated in Figs. 1(d) and 2(d). In addition, we can observe the temporal double-slit interference structure, which stems from the interference of the electron wave packet produced at the two adjacent half cycles. Figure 7(d) shows the PMDs are

mainly distributed in the region of $p_x \in [-1.0 \text{ a.u.}, 1.0 \text{ a.u.}]$ for $\varphi = 0.5\pi$. The PMDs also show the holographic interference structure in negative direction. Because of the change of the ionization channel, the motion of the rescattering electron will change. It is proved once again that the PMDs are very sensitive to the CEP.

IV. CONCLUSIONS

In summary, we investigate theoretically the photoelectron holography in strong-field ionization in a few-cycle chirped laser pulses. It is shown that the numerical results by solving the two-dimensional time-dependent Schrödinger equation (TDSE) are in agreement with that by using the semiclassical two-step (SCTS) model. We demonstrate that the PMDs in a negatively chirped laser pulse are more sensitive to the chirp parameters than those in a positively chirped laser pulse. In a negatively chirped laser pulse, the holographic interference structure can be isolated by adjusting appropriate negative chirp parameter ($\beta = -2$). We illustrate that the holographic interference structure comes from the rescattered electron wave packet ionized on the attosecond timescale. Our results may provide a reference for further research of the attosecond dynamics. In addition, we demonstrate that the chirped laser pulse not only can control precisely the opening or the closing of the ionization channel but also can be used to coherently control the recollision process. By analyzing the rescattered trajectory, we illustrate that the travel time of the rescattered electron is increased and the rescattered electron can obtain high return energy in a negatively chirped laser pulse. In addition, we also illustrate that the PMDs are very sensitive to the carrier-envelope phase.

ACKNOWLEDGMENT

This work was supported by the National Natural Science Foundation of China (Grant No. 12074142).

- [1] P. Agostini, F. Fabre, G. Mainfray, G. Petite, and N. K. Rahman, *Phys. Rev. Lett.* **42**, 1127 (1979).
- [2] L. V. Keldysh, *Zh. Eksp. Teor. Fiz.* **47**, 1945 (1964) [*Sov. Phys. JETP* **20**, 1307 (1965)].
- [3] G. G. Paulus, W. Nicklich, H. Xu, P. Lambropoulos, and H. Walther, *Phys. Rev. Lett.* **72**, 2851 (1994).
- [4] M. Ferray, A. L'Huillier, X. F. Li, L. A. Lompre, G. Mainfray, and C. Manus, *J. Phys. B: At., Mol. Opt. Phys.* **21**, L31 (1988).
- [5] X.-X. Huo, Y.-H. Xing, T. Qi, Y. Sun, B. Li, J. Zhang, and X.-S. Liu, *Phys. Rev. A* **103**, 053116 (2021).
- [6] Z. Shu, H.-J. Liang, Y.-C. Wang, S.-L. Hu, S. Chen, H.-F. Xu, R. Ma, D.-J. Ding, and J. Chen, *Phys. Rev. Lett.* **128**, 183202 (2022).
- [7] D. N. Fittinghoff, P. R. Bolton, B. Chang, and K. C. Kulander, *Phys. Rev. Lett.* **69**, 2642 (1992).
- [8] S. Ben, T. Wang, T.-T. Xu, J. Guo, and X.-S. Liu, *Opt. Express* **24**, 7525 (2016).
- [9] Y.-L. Wang, S.-P. Xu, W. Quan, C. Gong, X.-Y. Lai, S.-L. Hu, M.-Q. Liu, J. Chen, and X.-J. Liu, *Phys. Rev. A* **94**, 053412 (2016).
- [10] P. B. Corkum, *Phys. Rev. Lett.* **71**, 1994 (1993).
- [11] P. Salieres, B. Carré, L. L. Déroff, F. Grasbon, G. Paulus, H. Walther, R. Kopold, W. Becker, D. B. Milošević, A. Sanpera, and M. Lewenstein, *Science* **292**, 902 (2001).
- [12] X.-B. Bian, Y. Huismans, O. Smirnova, K.-J. Yuan, M. J. J. Vrakking, and A. D. Bandrauk, *Phys. Rev. A* **84**, 043420 (2011).
- [13] M. Richter, M. Kunitski, M. Schöffler, T. Jahnke, L. P. H. Schmidt, M. Li, Y. Liu, and R. Dörner, *Phys. Rev. Lett.* **114**, 143001 (2015).
- [14] J.-H. Chen, S. Ben, Q. Zhen, Y. Sun, and X.-S. Liu, *Opt. Express* **30**, 5095 (2022).
- [15] D. G. Arbó, K. L. Ishikawa, E. Persson, and J. Burgdörfer, *Nucl. Instrum. Methods Phys. Res., Sect. B* **279**, 24 (2012).
- [16] F. Lindner, M. G. Schätzel, H. Walther, A. Baltuška, E. Goulielmakis, F. Krausz, D. B. Milošević, D. Bauer, W. Becker, and G. G. Paulus, *Phys. Rev. Lett.* **95**, 040401 (2005).
- [17] Y. Huismans, A. R. e. A. Rouzée, A. Gijsbertsen, J. H. Jungmann, A. S. Smolkowska, P. S. W. M. Logman, F. Lépine,

- C. Cauchy, S. Zamith, T. Marchenko *et al.*, *Science* **331**, 61 (2011).
- [18] D. G. Arbó, K. L. Ishikawa, K. Schiessl, E. Persson, and J. Burgdörfer, *Phys. Rev. A* **81**, 021403(R) (2010).
- [19] Y. Li, Y.-M. Zhou, M.-R. He, M. Li, and P.-X. Lu, *Opt. Express* **24**, 23697 (2016).
- [20] M. Li, W.-C. Jiang, H. Xie, S. Luo, Y. Zhou, and P. Lu, *Phys. Rev. A* **97**, 023415 (2018).
- [21] Y. Sun, Z. Wang, X.-X. Huo, and X.-S. Liu, *Phys. Rev. A* **105**, 043115 (2022).
- [22] Z. Chang, A. Rundquist, H. Wang, I. Christov, H. C. Kapteyn, and M. M. Murnane, *Phys. Rev. A* **58**, R30 (1998).
- [23] J. Wu, G.-T. Zhang, C.-L. Xia, and X.-S. Liu, *Phys. Rev. A* **82**, 013411 (2010).
- [24] T. Nakajima, *Phys. Rev. A* **75**, 053409 (2007).
- [25] D. Zille, D. Adolph, M. Möller, A. M. Sayler, and G. G. Paulus, *New J. Phys.* **20**, 063018 (2018).
- [26] L.-Y. Peng, F. Tan, Q. Gong, E. A. Pronin, and A. F. Starace, *Phys. Rev. A* **80**, 013407 (2009).
- [27] Y. Xiang, Y.-P. Niu, and S.-Q. Gong, *Phys. Rev. A* **80**, 023423 (2009).
- [28] J. J. Carrera and Shih-I. Chu, *Phys. Rev. A* **75**, 033807 (2007).
- [29] Y. Pan, S.-F. Zhao, and X.-X. Zhou, *Phys. Rev. A* **87**, 035805 (2013).
- [30] P.-C. Li, X.-X. Zhou, G.-L. Wang, and Z.-X. Zhao, *Phys. Rev. A* **80**, 053825 (2009).
- [31] V. Tosa, H. T. Kim, I. J. Kim, and C. H. Nam, *Phys. Rev. A* **71**, 063807 (2005).
- [32] J. T. Lin and T. F. Jiang, *Phys. Rev. A* **63**, 013408 (2000).
- [33] D. S. Brambila, A. Husakou, M. Ivanov, and N. Zhavoronkov, *Phys. Rev. A* **96**, 063825 (2017).
- [34] N. I. Shvetsov-Shilovski, M. Lein, L. B. Madsen, E. Räsänen, C. Lemell, J. Burgdörfer, D. G. Arbó, and K. Tókési, *Phys. Rev. A* **94**, 013415 (2016).
- [35] M. D. Feit, J. J. A. Fleck, and A. Steiger, *J. Comput. Phys.* **47**, 412 (1982).
- [36] H.-D. Zhang, S. Ben, T.-T. Xu, K.-L. Song, Y.-R. Tian, Q.-Y. Xu, S.-Q. Zhang, J. Guo, and X.-S. Liu, *Phys. Rev. A* **98**, 013422 (2018).
- [37] M. Li, J.-W. Geng, H. Liu, Y. Deng, C. Wu, L.-Y. Peng, Q. Gong, and Y. Liu, *Phys. Rev. Lett.* **112**, 113002 (2014).
- [38] M. V. Ammosov, N. B. Delone, and V. P. Krainov, *Zh. Eksp. Teor. Fiz.* **91**, 2008 (1986) [*Sov. Phys. JETP* **64**, 1191 (1986)].
- [39] N. B. Delone and V. P. Krainov, *J. Opt. Soc. Am. B* **8**, 1207 (1991).
- [40] D. D. Hickstein, P. Ranitovic, S. Witte, X.-M. Tong, Y. Huismans, P. Arpin, X. Zhou, K. E. Keister, C. W. Hogle, B. Zhang, C. Ding, P. Johnsson, N. Toshima, M. J. J. Vrakking, M. M. Murnane, and H. C. Kapteyn, *Phys. Rev. Lett.* **109**, 073004 (2012).
- [41] H. Xie, M. Li, Y. Li, Y. Zhou, and P. Lu, *Opt. Express* **24**, 27726 (2016).
- [42] H. Liu, Y. Liu, L. Fu, G. Xin, D. Ye, J. Liu, X. T. He, Y. Yang, X. Liu, Y. Deng, C. Wu, and Q. Gong, *Phys. Rev. Lett.* **109**, 093001 (2012).
- [43] S. D. López and D. G. Arbó, *Phys. Rev. A* **100**, 023419 (2019).
- [44] M.-H. Yuan, A. D. Bandrauk, and X.-B. Bian, *Phys. Rev. A* **103**, 013108 (2021).